Spatial-temporal order-disorder transition in angiogenic NOTCH signaling controls cell fate specification

Tae-Yun Kang[1]*, Federico Bocci[2,3]*, Qing Nie[2,3], José Nelson Onuchic[4], Andre Levchenko[1]

*These two authors contributed equally to this work

[1]Department of Biomedical Engineering, Yale University
[2]NSF-Simons Center for Multiscale Cell Fate Research, University of California Irvine
[3]Department of Mathematics, University of California Irvine
[4]Center for Theoretical Biological Physics, Rice University
To whom correspondence may be addressed. Email: jonuchic@rice.edu
or andre.levchenko@yale.edu.

Abstract

Angiogenesis is a morphogenic process resulting in *de novo* formation of vascular beds, usually in hypoxic micro-environments. The initial steps of angiogenesis depend on robust differentiation of oligopotent endothelial cells into the Tip and Stalk phenotypic cell fates, controlled by Notch dependent cell-cell communication. The dynamics of spatial patterning of this cell fate specification are only partially understood. Here, by combining a controlled experimental angiogenesis model with mathematical and computational analyses, we found the regular spatial Tip-Stalk cell patterning can undergo an order-disorder transition at a relatively high input level of a pro-angiogenic factor VEGF. The resulting differentiation is robust but temporally unstable for most cells, with only a subset of presumptive Tip cells leading sprout extensions. We further find that sprouts form in a manner maximizing their mutual distance, consistent with a Turing-like model that may depend on local enrichment and depletion of fibronectin. Together, our data suggest that Notch signaling mediates a robust way of cell differentiation enabling but not instructing subsequent steps in angiogenic morphogenesis, which may require additional cues and self-organization mechanisms. This analysis can assist in further understating of cell plasticity underlying angiogenesis and other complex morphogenic processes.

Introduction

Angiogenesis, or *de novo* formation of blood vessels from the pre-exiting ones, is a striking example of phenotypic plasticity in an adult differentiated endothelium. Pro-angiogenic factors secreted in response to hypoxic conditions, particularly the vascular endothelial growth factor (VEGF), specify differentiation of endothelial cells lining blood vessels into diverse phenotypic states, particularly the Tip cell phenotype. Tip cells can initiate invasive cell migration into the surrounding extracellular matrix (ECM), leading to sprouting and branching of the nascent vessels(1, 2). Tip cells are differentiated from Stalk cells, another phenotypic state, through juxtacrine cell-cell interaction between these cell types involving Notch1 signaling, triggered and modulated by induction of Dll4 and Jag1 ligands(3, 4). Stalk cells can therefore form in immediate proximity of Tip cells, particularly, at the leading edge of an extending sprout, if the Notch signaling is sufficiently pronounced for the Tip-Stalk differentiation to occur. Proliferation of Stalk cells is as essential as the invasive migration of Tip cells for the emergence, extension and branching of growing sprouts, making the analysis of coordinated Tip and Stalk specification particularly important.

The inputs specifying the cell fate can be potentially contradictory, e.g., with pro-angiogenic factors, such as VEGF, promoting the Tip cell fate, and the Notch signaling activated by the neighboring cells promoting the Stalk cell fate and thus suppressing the Tip cell identity in the same cell. These and other signaling inputs can thus be incoherent in terms of cell fate specification and can result in complex dynamic outcomes that are still poorly understood. Further elucidation of these processes thus requires high resolution, quantitative experimental measurements tightly coupled with computational analysis. Since such measurements are still challenging *in vivo*, particularly in mammalian tissues, use of tissue models recapitulating the salient features of the developing vasculature is a key tool in the current analysis of angiogenesis and development of *de novo* vascular beds.

Previously, we and others have developed a set of micro-fabricated experimental angiogenesis models that have had progressively improved biomimetic characteristics(5-9). These characteristics include spatially and biochemically appropriate cell micro-environments, composed of components of the extracellular matrix and of gradients of growth factors and cytokines around the developing vasculature, of endothelial and mural cells. We have used this approach to map different combinations of VEGF and an inflammatory cytokine, TNF, onto pro- and anti-angiogenic outcomes, modeling frequently encountered angiogenesis conditions(7). A key to this analysis was a tight integration of quantitative experimental measurements with mathematical modeling that provided a systems level understanding of the intracellular signaling and cell-cell communication underlying angiogenic cell specification. A particularly interesting outcome of this analysis was the finding that pro-angiogenic stimuli lead to formation of both well-formed sprouts that were multi-cellular and had detectable lumens and to the emergence of single-cell extensions from the parental vessel. We termed these extensions ‘mini-sprouts’. Our analysis suggested that mini-sprouts were prospective Tip cells that however fail to lead the formation of full-fledged sprouts at the time of the measurement. However, the fate of these 'mini-sprouts’ and the overall dynamics of the Tip cell specification and sprouting are still not understood. Furthermore, although our analysis was successful in explaining the fraction of Tip cells formed under different conditions, it was not clear if the same mechanism could also account for the spatial aspects of the Tip cell and sprout specification, such as their mutual separation and density.

We addressed these challenges here by extending our analysis to higher temporal and spatial resolution, both in experimental and mathematical models of angiogenic sprouting. Surprisingly, we found that the formation of mini-sprouts was a highly dynamic process, in which they could both retract after extension and form full-fledged sprouts. Furthermore, the spatial positioning of mini-sprouts was well explained by the predicted locations of the Tip cells in our model but the model could not account for which of the mini-sprouts would become fully formed spouts. Further analysis revealed that the stable sprout formation from mini-sprouts can be enabled by the local fluctuations of the density of fibronectin, a key pro-angiogenic ECM component, leading to sparse patterns where sprouts tend to distance themselves from other fully formed sprouts. These results reveal some of the key mechanisms that may define the density of the angiogenically formed vascular beds under diverse conditions.

Results

Angiogenesis can be modeled in a 3D biomimetic experimental setup

To explore the properties of angiogenic patterning and cell fate specification, we used an experimental model previously employed to assess the crosstalk between pro-angiogenic and pro-inflammatory stimuli(7). In this experimental setup, angiogenesis occurs from a 3D parental engineered endothelial vessel embedded in the collagen matrix and exposed to exogenously supplied VEGF and other pro-angiogenic factors (Fig. 1A-B). In agreement with prior observations, we found that this setup resulted in formation of both single cell extensions into the matrix (previously classified as vascular mini-sprouts) and full-fledged multi-cellular sprouts containing detectable lumens and pronounced leading Tip cells (Fig. 1C). Sprouts displayed a variety of growth stages, including the very early ones, composed of one lumenized cell or pairs of connected cells, also forming a lumen (Table 1). Although mini-sprouts formed throughout the observation area of the vessel, sprouts developed within specific zones, while other zones remained devoid of detectable spout formation over the course of the study (Figs. 1D-F). These observations suggested that cell fate specification and sprout formation are dynamic processes that may display diverse local outcomes. We therefore set out to characterize these processes in the context of an accessible and well defined analysis tool that can allow to contrast experimental findings with mathematical models of angiogenic patterning, particularly those based on the commonly assumed Notch receptor mediated cell-cell interactions (Fig. 1G).

Mathematical model of VEGF/Notch signaling predicts spatially resolved Tip-Stalk patterns

To set the framework for the analysis of cell fate determination, we extended our previously developed and experimentally validated mathematical model of Tip-Stalk fate differentiation between two cells(10) to a multicellular hexagonal lattice in two-dimensions. In the new model, we replicated within each cell the signaling network incorporating the Notch and VEGF pathways (Fig. 2A). Prior analysis of this model on the level of two adjacent cells predicted the emergence of bistability between a (high Notch, low Delta) Stalk phenotype and a (low Notch, high Delta) Tip phenotype(10). This result is consistent with the overall expectation of the differentiation effect of Delta-Notch signaling, which in 2D is further expected to generate 'salt-and-pepper ' patterns, with a single Tip cell surrounded by 6 Stalk cells (11), yielding the overall fraction of Tip cells in this arrangement of 25%. However, this simple bistability and spatial patterning picture

can be altered by signaling inputs that potentially conflict with those involved in Delta-Notch signaling (Fig.1G). For example, the VEGF pro-angiogenic factor promoting the Tip cell fate, can conflict with the Notch signaling activated by the neighboring cells that instead promotes the Stalk cell fate while suppressing the Tip cell identity. This might result in disordered patterns with adjacent Tip cells that deviate from the archetypical salt-and-pepper configuration. To explore the properties of this disordering effect, we ran simulations, in which the VEGF-Notch signaling occurred in all individual cells within a hexagonal array of the model multi-cellular endothelium, starting from randomized initial conditions (Fig. 2A). The fully equilibrated patterns were then analyzed for distributions of the simulated Delta and Notch expression across the cells. We found that for a wide range of VEGF inputs, the distributions of Delta and Notch displayed largely bimodal distributions, and the levels of the average Delta expression increased with the increasing input (Fig. 2B-C, supplementary Fig. 1A-B) due to positive regulation of the activated VEGF receptor on Delta (see again the circuit in Fig. 2A). Nevertheless, the clear overall bimodality allowed us to consistently classify cells into the Delta-high ('Tip') and Delta-low ('Stalk') cell states and examine the spatial distribution of these cellular sub-types (see Method section: Mathematical model of VEGF/Notch signaling).

The spatial Tip-Stalk cell distribution patterns revealed a complex dependency on the VEGF input. At relatively low VEGF levels, the patterns were mostly ordered, with small deviations from the expected 'salt and paper 'geometry with a 25%-75% ratio of tip-stalk (Fig. 2D). However, as the VEGF input increased, the fraction of tips grew and the patterns became sharply more disordered over a relatively narrow range of magnitude of the VEGF input, and then became progressively further disordered, but with a lower VEGF sensitivity, over several more orders of magnitude of VEGF inputs (Fig. 2D-E and supplementary Fig. 1A-B). Spatial patterns in the disordered phase at high VEGF input levels were characterized by much higher fractions of Tip cells that were frequently in contact with each other as quantified by a "disorder index" (supplementary Fig. 1C-D). This transition was reminiscent of the order-disorder transition commonly observed and studied in the change of the order of atoms in various substances as a function of temperature, and in other chemical systems (12, 13). As expected for these types of transitions, increasing or decreasing the order-stabilizing Delta-Notch cell-cell signaling, resulted in the corresponding shifts of the ranges of VEGF inputs, over which the sharp order-disorder transition occurred. For example, a small increment or decrease in the cellular production of the Delta ligand shifted the order-disorder transition to either lower or higher VEGF inputs (Fig. 2F). As the broad sweep of the VEGF inputs simulated in the mathematical model is likely beyond the range of receptor sensitivity for the experimental VEGF signaling, we contrasted the predicted fractions of Tip cells with the previously made observations in the 3D experimental angiogenesis model shown in Fig. 1. We found that, for the VEGF = 10 ng/ml, the experimentally determined fraction of the Tip cells was 0.20 ± 0.08 (mean$\pm$ SD), i.e., encompassing the fraction of 0.25 expected for the completely ordered, 'salt-and-pepper 'Tip cell distribution pattern. However, for VEGF = 100 ng/ml the experimentally observed Tip cell fraction was 0.32 ± 0.01 (mean$\pm$SD), which corresponded to the disordered state predicted by the model under higher VEGF inputs. We therefore concluded that the transition between order and disorder can occur in the 10-100 ng/ml range of VEGF concentration, allowing us to investigate the properties of the disordered state and its relationship to the spatial frequency of sprout formation. Based on the Tip/Stalk cell ratio, we calibrated the model's parameters so that a VEGF input of 100 ng/ml matched the experimentally observed

Tip/Stalk fractions at the same experimental VEGF input (see Methods section: Mathematical model of VEGF/Notch signaling).

Precise quantification of Tip cell spatial arrangement suggests disordered patterning in the engineered angiogenesis model

To enable the comparison between the modeling predictions and experimental observations, we quantified the spatial patterning characteristics of the inferred positions of the Tip cells in the experimental angiogenesis model. As in our prior analysis using this experimental approach (7), we identified Tip cells based on their key *phenotypic* characteristic — invasive migration into the surrounding collagen matrix. These cells either can be present in the form of 'mini-sprouts', i.e., single Tip cells invading into the matrix from the parental vessel, or tips of single- or multicellular sprouts containing recognizable lumens (see Fig. 3A for examples of this classification). As indicated above, in this classification, sprouts could be composed from as few as a single cell, if this cell, invaded the matrix also displayed an identifiable lumen. Since both these structures involved Tip cells specified in the monolayer of endothelial cells that lined the parental vessel, we constructed a two-dimensional map of the inferred spatial positions of Tip cells at the location of all mini-sprouts and sprouts (Figs. 3A & B). This mapping (see Methods section: Quantification of Tip-Tip distance in experiments) assumed that the Stalk cells found in the extending sprouts emerge *de novo* through cell proliferation, rather by Stalk cell migration from the parental vessel. Experimentally, we used nuclear staining to identify non-Tip cells. Since the results above suggested that the cell fates and their patterns in our experimental setup were consistent with the ordered or somewhat disordered 'salt-and-paper 'patterns, we further assumed that all the non-Tip cells adopted the Stalk fates (in the sense of Delta-low, Notch-high status, alternative to the Tip cell fate). The resulting map of experimentally specified Tip and Stalk cell locations was then used to calculate the shortest distances between Tip cells, measured in 'cell hops', i.e., the minimal number of intermediate cells between randomly chosen pairs of Tip cells (Fig. 3B). These distances included Stalk cells exclusively, and no intermediate Tip cells. If two or more Tip cells were at equal distance from a given other two cell, their distance ranking was assigned randomly (e.g., two Tip cells at the equal minimal distance to a given Tip cell, would be randomly assigned the ranking of the closest and second closest Tip cell). We then analyzed these data for the $VEGF_{EXT}$= 100 ng/ml experimental input which resulted in the most robust sprouting, contrasting the results with the predictions of our mathematical model for the same input level that, when averaging over multiple simulations, reproduced the same fraction of Tip cells. Finally, we computed a statistic of the shortest paths separating Tip cells in the equilibrated patterns (Fig. 3C and Methods section: Quantification of Tip-Tip distance in modeling). First, we determined the average distances from the Tip cells to the closest, second closest, etc. neighboring Tip cells. We found that this distance distributions closely agreed with the modeling predictions, particularly for the distances up to the 4th closest neighbor, differing substantially from the predictions for the ordered 'salt-and-pepper 'patterns (Fig. 3D). A key finding was that, in agreement with the expectation from the disordered pattern model, there were frequent cases of direct contact between two Tip cells, making the average distance to the closest Tip cell around 0.5 cells in the model. In contrast, two Tip cells were always separated by at least one Stalk cell in "traditional" 'salt-and-pepper 'models. Further analysis of the experimental distributions of Tip cell distances revealed that Tip cells were adjacent to at least 1 other Tip cell with 80% chance, and with at least 2 other Tip cells with 40% chance, and with at least 3 other Tip cells with 20% chance (Fig. 3E). These

Tip cell distance distributions were again in agreement with the modeling results, further supporting the predicted disordered pattern of cell specification.

Dynamic tracking of angiogenic cell fate specification

The integrative, computational and experimental, analysis presented above suggested that the spatial Tip cell distribution can be well explained by the model of a partially disordered 'salt-and-pepper' mechanism. However, it is not clear whether all such Tip cells would spearhead the formation of a new sprout, or retract back to an alternative (Stalk) cell fate. From the experimental perspective, this question can be addressed by temporal tracking of the fates of mini-sprouts to examine whether this state is an intermediate step towards the sprout formation. To study this question, we imaged the progress of sprouting in the same areas of a live parental vessel at different time points of 1 hour, 3 hours, 7 hours and 28 hours of incubation in 100 ng/ml of VEGF (Fig. 4A-H). Strikingly, we found that although all sprouts indeed formed from mini-sprouts, not all mini-sprouts persisted and initiated sprout formation. Instead, many mini-sprouts retracted and new mini-sprouts formed during the time-course of the analysis. We then tracked a group of 118 cells which adopted the mini-sprout phenotype at least once over a period of 28 hours after VEGF exposure. Their state change dynamics was visualized using the Sankey diagram (Fig. 4I). The initial state of any sprouts or mini-sprouts was considered to be that of the Stalk cell to reflect the hypothesized 'salt-and-pepper 'patterning structure, entirely consisting of either Tip or Stalk cells. When a mini-sprout retracted, it was newly marked as a Stalk cell. By the final time point of 28 hours of VEGF exposure, 45.8% of the cells that displayed the mini-sprout phenotype at least once during the experiment retracted back to the Stalk state, illustrating the highly dynamic phenotype of mini-sprout extensions and retractions. Of the remaining cells, 41.5% and 12.7% were classified to be either in the mini-sprout or sprout-leading Tip cell states, respectively. Although sprout formation continued throughout the experiment, the rate of conversion of mini-sprouts to full-fledged sprouts gradually decreased over time, with 13.6%, 2.9%, and 7.5 % of mini-sprouts becoming sprout-leading Tip cells in the time ranges of 1-3, 3-7 and 7-28 hours. respectively (Fig. 4K-M). In most cases (86.7%), spouts emerged from *newly formed* mini-spouts (i.e., the cells that were Stalk cells and then mini-sprouts in the preceding two time points), suggesting that mini-spouts represent transient states rapidly converting to either the fully committed sprout state or to the Stalk state (Fig. 4 O). These observations raised the question of what might define the commitment of a mini-sprout to the sprout differentiation. We next addressed this question by analyzing the spatial distribution of fully formed sprouts over the observed area of the parental vessel.

Random uniform model accounts for spatial distribution of extending sprouts

While the Notch/VEGF mathematical model could quantitatively resolve Tip-Stalk spatial patterns, and dynamical cell tracking quantified the rates of cell state switching, it is unclear how to predict mini-sprout/sprouts fate commitment based on Notch/Delta molecular expression. To identify the underlying principles of sprout initiation, we thus integrated the multicell model with different phenomenological hypotheses (summarized in Fig. 5A-D). Testing of these hypotheses was based on the measured distributions of distances between sprouts and, in particular, the observation that sprouts were always separated by at least one non-sprout cell (blue bars in Fig.

5E). We tested the models mathematically, ensuring that the results were normalized to the overall density of sprouts observed experimentally (see Method section: Phenomenological models of Sprout selection). The first straightforward hypothesis was that mini-sprouts commit to the sprout phenotype independently of the location of other forming sprouts, constituting the "cell-autonomous sprout selection" model (Fig. 5A-B). In this case, however, the corresponding model predicted multiple contacts between sprouts (black line in Fig. 5E), in sharp contrast with the experimental observation. The observation that most sprouts are in contact with at least another Tip (Supplementary figure 2A), but never in contact with another sprout, suggested a control mechanism where sprout selection inhibits nearby Tip cells from committing to the same fate. To test this hypothesis, we set up two additional phenomenological models of sprout selection. First, a "repulsion between sprouts" model where sprouts cannot be in contact; therefore, Tip cells cannot commit to the sprout phenotype if already in contact with a sprout (Fig. 5C). Second, a "random uniform" model where sprouts are selected randomly, but maximizing their overall spread in the lattice (Fig. 5D). These models of sprout selection were tested starting from the equilibrated Tip-Stalk multicellular patterns predicted by our Notch-VEGF mathematical model, and randomly assigning the "Sprout state" to Tip cells until the experimental sprout density was reached (see Method section: Phenomenological models of Sprout selection). While both models correctly predicted sprouts to never be in contact, the "random uniform" model better described the cases where adjacent sprouts are separated by two or more cells (Fig. 5E).

To test these mechanisms more rigorously, we computed the average distance (in cell numbers) between pairs of closest sprouts while also varying the number of sprouts allowed in the lattice (supplementary figure 2B-D), thus generating a curve of the typical sprout-sprout distancing as a function of sprout density in the lattice (Fig. 5F). The "random uniform" model predicts very closely the experimentally observed combination of sprout fraction and sprout-sprout distance, whereas the other two models greatly underestimated the distances between sprouts (Fig. 5F). Furthermore, while all models overestimated the fraction of the adjacent sprouts that are one cell away from the current sprout and underestimated the fractions of sprouts at greater distances, the deviation of the "random uniform" model predictions for this inter-sprout distribution was the lowest of all the models, again supporting the 'random uniform' model as the more likely to account for sprout selection (Fig. 5F). Interestingly, the random uniform model further suggests a very sharp transition between sparse and dense sprout patterns that is triggered by the increase of sprout density in the lattice (Supplementary Fig. 3), a further prediction that could be tested in the future to validate the proposed mechanism.

Fibronectin distribution may mediate sprout induction

Random distribution maximizing the distance between sprouts is similar to allelopathy models, accounting to spatial dispersion of species maximizing distance between them. In these models, the key postulated mechanism is inhibition of growth of individuals of the same species through a mutual suppression mechanism(14-16). Another analogous set of mechanisms are embedded within the concept of Turing pattern formation, the key to which is diffusible negative feedback regulator setting spatial distribution of morphogenic features (17, 18). A variant of such mechanisms is a model postulating depletion of some ingredient that is key to the local growth, by its active redistribution towards the growing pattern features and depletion from the zones between them, rather than active mutual inhibition of the pattern forming units.

Given these prior models, we hypothesized that a similar mechanism may account for the dispersion patterns of sprouts. We focused on the extracellular matrix as a possible medium accounting for the positive and negative pattern-setting interactions. Indeed recently, it has been observed that collagen can be re-organized by the growing sprouts, so that it is concentrated around the extending sprouts and depleted elsewhere(19-21). We explored whether a similar distribution is also be observed for fibronectin, an ECM component that may be consequential to the angiogenesis processes. Fibronectin expression levels in the vicinity of individual cells comprising the parental vessel and the emerging sprouts was experimentally assessed by immunostaining, with simultaneous cell identification using induced cytoplasmic GFP expression and nuclear staining, followed by 3D reconstruction (Figs. 6A-H). Untreated quiescent cells (No treatment) and mini-sprouts showed similar levels of fibronectin expression (Fig. 6H). Interestingly, the fibronectin expression was highly enriched at the base but not the tip areas of the extending sprouts, suggesting that it may be a key determinant of sprout induction but not extension (Figs. 6B,C, &H).

The fibronectin expression levels around individual cells were highly variable and not necessarily indicative of the overall regional variation of the levels of this ECM protein. To examine variation of fibronectin expression in larger areas, we accessed the ratio of cells having fibronectin levels higher than a threshold in groups of 7 cells around sprouts and mini-sprouts (Figs. 6I &J). The overall expression levels when all region types were combined was relatively uniform (Fig. 6J, third panel. Strikingly however, regions around sprouts (Fig. 6J, first panel) and mini-sprouts (Fig. 6J, second panel) showed oppositely skewed patterns. There was an enrichment of cells around sprouts that expressed fibronectin levels higher than the threshold, whereas cells around mini-sprouts tended to express fibronectin levels lower than the threshold. Altogether, these results supported the model in which fibronectin can indeed serve as a mediator of Turing-like induction of spouting patterns, through re-modeling that enriches it at the points of sprout induction and depletes it at the points where Tip cells (mini-sprouts) are not stabilized to form full-fledged, lumenized sprouting bodies.

Discussion

A major challenge of the analysis of tissue development and homeostasis is the understanding of how differentiation into distinct cell types can be robustly achieved, while also being sensitive to various pro-differentiation and morphogenic cues and, potentially affected by molecular noise in biochemical reactions. In the context of angiogenesis, this challenge relates to vascular morphogenesis and the co-occurring robust differentiation of endothelial cells into Tip and Stalk cells states. This process is guided by the multiple pro-angiogenic cues, such as VEGF and by the local tissue organization and mediated by the paracrine Delta-Notch cell signaling. Recent mathematical models of this process(22, 23) have considered the robustness of the Delta-Notch differentiation to molecular noise, concluding that noisy biochemical reactions can both disrupt and enhance the spatial differentiation patterns, depending on the magnitude and spatial distribution (22). The effect of pro-angiogenic cues, such as VEGF on robustness of spatial differentiation patterning remains substantially less explored. Furthermore, compiling between modeling predictions and experimental validation has been challenged by the complexity of *in vivo* angiogenesis analysis, both on cellular and molecular levels.

Here, we integrated engineered experimental angiogenic assay with a spatially resolved computational modeling analysis to explore the spatially and temporally resolved effects of VEGF on angiogenic cell speciation. Our results suggest that VEGF can have a dual role in inducing the initial Tip-Stalk cell differentiation. On the one hand, a low level of exogenous VEGF is essential to induce Delta-Notch signaling and the classical ordered 'salt-and-pepper' pattern, with approximately 25% of the cells adopting the Tip cell fate, as expected (24). This role of VEGF is conceptually similar to the classical case of EGF induced Notch signaling in C. elegance vulva development (25, 26). On the other hand, our results also suggest that an increase of VEGF levels can introduce disorder into this pattern, similar to order-disorder transition for various composite materials (12, 13), which may occur with increasing temperature and have the properties of a sharp phase transition. More specifically, high VEGF levels may play the role similar to an increased temperature in order-disorder transitions, leading to emergence of partially disordered 'salt-and-pepper 'structures. These disordered structures are characterized by higher than expected fractions of Tip cells and, consequentially, an increased occurrences of otherwise disallowed adjacent Tip cells. Importantly, for all VEGF input levels and the resulting spatial patterns, the Tip-Stalk cell specification continued to be robust, although the degree of induction of Notch signaling was dependent on the VEGF dose. These results suggested that cell specification patterns deviating from the expected 'salt-and-pepper' one can develop not only due to noisy Notch signaling, as suggested by prior models, but also due to an increase in the fraction of a specific resulting cell state by an elevated magnitude of the input of the pro-differentiation cue.

In spite of the observation that disordered 'salt-and-pepper' patterns still display robust differentiation, the spatial patterns of cell co-localization can generate inherent instabilities, e.g., due to two adjacent Tip mutually suppressing their fate selection through Notch signaling. Instabilities of this sort may increase the sensitivity of the differentiation process to additional cues and can also lead to facilitated dynamic switching of cell fates (e.g., Tip to Stalk and vice versa) over prolonged periods of time. Such instabilities might lead to oscillatory-like fluctuations of Notch signaling as observed in other differentiation processes (27-29) and in endothelial cell sheets under high VEGF concentration inputs(30). Importantly, these instabilities may also underlie the continuous retraction and extension of mini-sprouts observed in our study. This dynamic fate-switching behavior can thus represent a signature of unstable differentiation process that may either stabilize, leading to a specific morphogenetic outcome, such as extension of a stable sprout, in response to additional cues, or display a prolonged instability resulting in a lack of pronounced morphogenesis. Such poised but unstable states may be similar to the undifferentiated state of neurogenic progenitors displaying oscillatory Notch signaling, which can proceed to differentiation after the oscillation is resolved into a temporally stable Notch activity (31).

The cues stabilizing cellular differentiation and morphogenesis can vary and represent the signature of both global and local pro- and anti-angiogenic environments. For instance, our prior analysis indicated that exposure of model parental vessels to VEGF only rather than a more complete pro-angiogenic cocktail of various factors, can result in formation of mini-sprouts (and hence, effective Tip-Stalk cell differentiation), but not full-fledged sprouts (7). Sprout formation may also be modulated by the presence of mural cells and pro-inflammatory cytokines, which can indirectly modulate the Notch activity, but could also have additional effects, serving to stabilize a specific differentiation outcome. However, even if sprouts do form, it is not clear how their spatial distribution may arise and be potentially controlled by the environmental inputs. Our results

argue that, for a given number of sprouts forming in the parental vessel, their mutual distances are maximized. This spatial distribution is consistent with a Turing-like mechanism (17, 18), implying the existence of a long-distance interaction inhibiting formation of new sprouts in the vicinity of the existing ones. Although the actual mechanism of putative Turning-like pattern formation is not fully elucidated here, our results are consistent with a variant of this regulatory behavior, in which a component of the extracellular matrix, fibronectin is actively redistributed by the nascent sprouts, enriching this ECM component at the points of sprout formation, while also depleting it from other zones, thus preventing sprout induction in the depleted areas. This redistribution is indeed equivalent to the classical Turing mechanisms that would involve generation of an explicitly inhibitory compound by the growing sprouts. Fibronectin has been implicated as a pro-angiogenic ECM component, possibly due to its integration with VEGF, which further increases the plausibility of this mechanism (32). Consistent with this putative mechanism, we find elevated levels of fibronectin at the bases of extending sprouts, but not at their tips. This finding has two implications. First, fibronectin may be an important factor in the sprout induction rather than extension, hence the growing sprout can progress into the surrounding matrix beyond the area of enriched fibronectin, leaving it behind. Secondly, fibronectin can also promote lumen formation (33, 34), thus its enrichment at the bases of extending sprouts can further contribute to their lumenized structure. Furthermore, this mechanism can help explain the dramatic influence of cytokines, such as TNF, in preventing sprout formation, which can happen in sharp, TNF dose-dependent manner (7). Indeed, TNF avidly binds to fibronectin (35) and therefore, at high enough concentrations, would have a particular anti-angiogenic effect in the areas of increased fibronectin density, which according to the proposed mechanism would be the areas of incipient sprouts. This would dramatically increase its anti-sprouting effect, even if the effect of this cytokine on the Notch-dependent cell specification is more muted (7). Of note, another version of the Turing mechanism has recently been suggested to account for the branching of the sprouts, also involving formation of new Tip cells leading individual branches, although the molecular mechanism postulated in that analysis was distinct from the one proposed here (36, 37). These models, though plausible, will need to be further tested to ascertain causality of the proposed mechanisms, although at this stage the Turing-like mechanisms appear to be the best candidates to explain the experimental results we obtained.

Overall, our analysis supports the following dynamic view of angiogenic induction. The VEGF input can induce Notch signaling and formation of Tip cells that can behave as mini-sprouts. At lower VEGF input, a more ordered pattern of Tip cell induction can lead to formation of approximately 25% of Tip cells, but relatively few of these will become sprouts, reflecting lower sensitivity to additional ambient cues, promoting sprout formation. On the other hand, at higher VEGF inputs, a greater disorder of Tip cell patterning permits higher sensitivity to external cues, such as fibronectin, that can stabilize the sprouting. In addition, a more frequent co-localization of Tip cells under this condition enables initiation of a sprout from two adjacent cells, as observed in a fraction of cases in our experiments. The initial emergence of sprouts leads to a progressively less likely sprout formation and to the overall maximization of the distance between the sprouts. Both these observations consistent with non-local inhibition of sprout formation around the sprouts that have already formed. A plausible mechanism for this inhibition and the overall pattern formation is the re-distribution of fibronectin from the zones between sprouts towards the incipient sprouts, constituting both a positive and negative feedback loops, commonly assumed in a variant of the Turing patterns from action. This mechanism is likely to be very sensitive to various local

inputs distinct from VEGF and fibronectin, which can further influence the location and density of the developing blood vessels. These may include the effects of pericytes or local inflammatory environments, as mentioned above, but also other ECM components, such as collagens, that may enhance the protrusion of Tip cells and thus stabilize the emergent sprouts both directly and indirectly. Endothelial fate induction process may be interesting to contrast with other complex multicellular processes, including collective epithelial migration, where Notch signaling similarly modulates fine-grained patterns of leader and follower cells (38), and underscore the need in the future to develop more refined models that explicitly integrate the interconnections between biochemical and mechanical regulation of Tip-Stalk fate(39).

The analysis presented here also further highlights the utility of combining experimental engineered vasculature models with mathematical analysis as integrated platforms to gain a progressively better insight into angiogenesis in highly controlled micro-environments. Although, many questions remain about the mechanistic underpinnings of the phenomena observed here and in related studies, the analysis enabled by these model systems can help formulate guiding hypotheses for further understanding of angiogenesis *in vivo*, while decoupling the complexities of the native angiogenic environments. We anticipate that the dynamic exploration presented here can help pave the way for further quantitative understanding of this key biological process.

Methods

Fabrication of 3D vessel chip

Chips for mimicking 3D angiogenesis in vitro were fabricated as introduced in our previous work(7). The chip for live-cell imaging consists of a PDMS chamber, an engineered blood vessel embedded in collagen gel, and the whole construct was placed on a glass-bottom dish (Fig. 1A). A single line mold (D: 200 -250 um, L: 10 mm) of PLA which has a semicircular cross-section was deposited on a petri dish with a 3D printer (Ultimaker). After a PDMS chamber was put on the mold, pre-mixed collagen solution (5mg/ml, Type 1 collagen, BD) according to manufacturer's protocol was injected through a hole on the PDMS chamber and collagen polymerization was induced on ice for 30 min and at 37 ℃ for 1.5 hours. The PDMS chamber including the collagen construct was carefully peeled off, then the bottom side was sealed with a glass bottom of a dish. Laminin solution (60ug/ml in PBS, Sigma Aldrich) was injected into the channel pre-made in collagen, then the chip was flipped upside down and incubated at 37 ℃ for 1 hour. Finally, endothelial cell suspension (1×10^7cells/ml) was injected into the channel, then the chip was flipped upside down again and incubated at 37 ℃ for 1 hour to allow cells to attach to the lumen. Once endothelial cells form a confluent monolayer on the channel surface, a fresh medium was injected into the engineered blood vessel and changed every 12 hours before the treatment with pro-angiogenic factors.

Cell culture and induction of angiogenesis

GFP-expressing human brain endothelial cells were purchased from Angio-Protemie and cultured in a growth medium of M199 (Gibco) supplemented with 20% FBS (Life Technologies), 1% HEPES (Thermo Scientific), 1% Glutamax (Thermo Fisher), 1% antibiotic-antimycotic (Thermo

Fisher), Heparin (25mg/500ml, Sigma Aldrich), and endothelial cell growth supplement (Sigma Aldrich). For inducing angiogenesis in the 3D vessel chip, the growth medium was supplemented with 40ng/ml of basic fibroblast growth factor (bFGF, Thermo Fisher), 500nM of Sphingosine-1-phosphate (S1P, Sigma Aldrich), and 75ng/ml of phorbol myristate acetate (PMA, Sigma Aldrich). And 100 ng/ml or 10 ng/ml of VEGF was added on the top reservoir of the 3D vessel chip to create a VEGF gradient toward the engineered blood vessel (Fig. 1B).

Mathematical model of VEGF/Notch signaling

We generalize existing mathematical models of the interconnected signaling between the Notch and VEGF pathways to a two-dimensional multicellular scenario (7, 40). The temporal dynamics of Notch (N), Delta (D), Jagged (J), Notch intracellular domain or NICD (I), and VEGF receptor (V_R) in a cell are modeled with ordinary differential equations:

$$\frac{dN}{dt} = N_0 H^+(I) - k_T N(D_{EXT} + J_{EXT}) - k_C N(D + J) - \gamma N \quad (1a)$$

$$\frac{dD}{dt} = D_0 H^-(I) H^+(V_R V_{EXT}) - k_T N_{EXT} D - k_C N D - \gamma D \quad (1b)$$

$$\frac{dJ}{dt} = J_0 H^+(I) - k_T N_{EXT} J - k_C N J - \gamma J \quad (1c)$$

$$\frac{dI}{dt} = k_T N(D_{EXT} + J_{EXT}) - \gamma_I I \quad (1d)$$

$$\frac{dV_R}{dt} = V_{R0} H^-(I) - k_T V_R V_{EXT} - \gamma V_R \quad (1e)$$

Notch, Delta, Jagged, and VEGF receptor are produced with basal rates N_0, D_0, J_0, V_{R0} and are degraded with rate constant γ. The basal production rates are modulated by NICD that transcriptionally activates Notch and Jagged while inhibiting Delta and VEGFR via shifted Hill functions:

$$H^S(I, I_0, n, \lambda) = \frac{1 + \lambda \left(\frac{I}{I_0}\right)^n}{1 + \left(\frac{I}{I_0}\right)^n} \quad (2)$$

Where I_0 is a threshold NICD level, n is the Hill coefficient, and λ represents the target's production rate fold-change at high NICD concentrations ($I \gg I_0$). Therefore, $\lambda > 1$ implies transcriptional activation while $\lambda < 1$ implies transcriptional inhibition. For brevity, activating and inhibiting Hill functions are denoted by $H^+(I)$, $H^-(I)$, respectively.

Receptors and ligands can bind to external ligands/receptors with binding rate constant k_T. In the case of Notch signaling, N_{EXT}, D_{EXT}, and J_{EXT} represent the average levels of Notch, Delta and Jagged in the six nearest neighbor cells on the hexagonal lattice. Conversely, VEGF is modeled as an external signal provided to all endothelial cells; therefore, all cells are exposed to the same fixed level (V_{EXT}). Moreover, Notch receptors and ligands can bind within the same cell with a rate constant k_C, which results in the degradation of the ligand-receptor complex without any downstream signaling (cis-inhibition). NICD is released upon binding of Notch receptors with external ligands and degraded with rate constant γ_I. Finally, VEGF receptors can bind to external VEGF ligands, thus creating activated VEGF receptor ($V_R V_{EXT}$), which in turn inhibits the production of Delta. Details on parameter values are presented in Table 2. Compared to previous

models, we rescaled the Hill function threshold for VEGF-mediated activation of Delta in order to match quantitatively the ratio of Tip/Stalk cells between model and experiment when the external input is $V_{EXT} = 100$ ng/ml.
In this project, we focus specifically on the regulation of VEGF on the Notch-Delta signaling pathway (as shown in Fig. 2A). A strong Notch-Jagged interaction can suppress Tip-Stalk differentiation and instead lead to a hybrid Tip/Stalk phenotype, which is beyond the scope of the current study. For completeness, we maintained the integrity of the entire circuit structure including Notch-Jagged interactions (eq. 1c) but fixed the production rate of Jagged at a low level that does not interfere with the bistable behavior of the VEGF/Notch circuit.

Simulation details
All results are calculated on a 30x30 hexagonal lattice with periodic boundary conditions. Initially, the lattice is prepared with randomized initial conditions where the initial levels of N, D, J, I, and V_R within each cell are sampled from uniform distributions. Afterwards, the lattice equilibrates for 100 hours without any VEGF input to simulate the seeding of endothelial cells before VEGF is provided.

Quantification of Tip-Tip distance in experiments
Fluorescence microscopy images of DAPI/phalloidin staining from our previous work(7), two images for each VEGF condition, were used to quantify the distance between Tips. Before counting Tip-Tip distance, images were pre-processed to clean up intricate 3D images as depicted in Figure 3A with IMARIS(Bitplane). First, all newly formed vessels were separated from parental vessels, identified as surface entities, and labeled with different colors depending on lumen formation: red for sprout and blue for mini-sprout. And all nuclei were detected as spots (Fig. 1A, Label nuclei on the parental vessel and Tip region). In this step, nuclei on the parental vessel region were marked as Stalks and the nuclei in sprout or mini-sprout surfaces were marked as Tips. Second, the nuclei of Stalks on the parental vessel region were re-examined (Fig. 3A, Re-label Tip and Stalk nuclei). If they are connected to sprout or mini-sprout surfaces (Fig. 3A (1) & (2)), they were re-labeled as nuclei of sprouts or mini-sprouts and all other nuclei in the sprout or the mini-sprout were deleted. If a nucleus of a sprout or a mini-sprout is not in the parental vessel, the closest nucleus to the parental vessel was labeled as a sprout or a mini-sprout and all other nuclei were deleted (Fig. 3A (3)). By going through these steps, we could derive 2D conceptual Tip-Stalk arrangements from 3D images, which are comparable to 2D Tip-Stalk patterns from mathematical modeling. The pre-process is based on our assumption that the Stalk cells found in the extending sprouts emerge *de novo* through cell proliferation, rather by Stalk cell migration from the parental vessel.
In this study, we defined the distance between two Tips as the number of cells measured in 'cell hops', i.e., the minimal number of intermediate cells between randomly chosen pairs of Tip cells. For example, in Figure 3B, the distances from Tip 1 to Tip 2 and to Tip 3 are 0 and 1, respectively. From Tip 1 to Tip 4, the distance is 3 in the minimal cell hops marked with gray arrows which pass through another Tip. Another cell hops marked with red arrows does not include any Tips, but the distance is 4. In this case, we discarded Tip 4 in the quantification of Tip-Tip distance from Tip 1. The same rule was applied in analyzing Tip-Tip distance from mathematical modeling (Figure 3C).

Quantification of Tip-Tip distance in modeling

Upon complete lattice equilibration, cells naturally separate into two distinct groups based on low or high expression of Delta irrespectively of the external VEGF input (see Fig. 2B). Therefore, high-Delta cells are labeled as tips and low-Delta cells are labeled as stalk. The algorithm to compute distances between tip cells on the hexagonal lattice follows the following two steps: (1) Computing the shortest path between a given pair of cells on the hexagonal grid; and (2) filtering out the measurement if the cell pair is 'shielded' by another tip cell. First, the shortest path is defined as the minimum number of intermediate cells that connect the two cells of interest. Considering two cells with coordinates (x_1, y_1) and (x_2, y_2), their distance has different values based on the cells relative position. In the simple case where $dx = 0$ or $dy = 0$, the distance is $d = dx + dy$. Else, if the distance is $d = dx + dy - 1$ (1) if dy is even of (2) if dy is odd but y_1 is even. In any other case, the distance is $d = dx + dy$. Next, to maintain consistency with the experimental statistics, the distance is not included in the tip cell distribution if there is at least one intermediate tip cell 'shielding' the two tip cells of interest. In the experimental protocol, an intermediate cell 'shields' the two tip cells if the straight line connecting the centers of the two cells passes through the shielding cell. Therefore, we search the intercept between the line connecting the pair of tip cells and a circle centered at the position of the shielding cell with radius of 0.5. Assuming a circular geometry for the shielding cell removes artifacts emerging due to the polygonal shape of cells in the hexagonal lattice. The Sprout-Sprout distance statistics presented in Fig. 5E are similarly computed by applying the same algorithm to the set of Sprout cells in the lattice (see the following section for details of Sprout selection).

Phenomenological models of Sprout selection

We developed three separate models of sprout selection: "Cell-autonomous", "Repulsion", and "Random uniform distribution". For all three cases, cells equilibrate in the hexagonal lattice. Then, tip cells are defined based on high-Delta expression. This analysis produces a discrete snapshot of Tip and Stalk cells on the hexagonal lattice. When comparing the model prediction to the 100ng/ml VEGF dosage experiment, we constrain the Sprout selection models to reproduce the experimental Sprout fraction. In the "Cell-autonomous" model, a fraction of the Tip cells is randomly selected and defined as Sprouts independently from the phenotype of their neighbors. In the "Repulsion" model, a fraction of Tip cells is randomly selected as Sprouts with the additional constraint that Sprouts cannot be in direct contact. To implement this constraint, we iteratively select Tips one at a time. If the selected Tip is not already in contact with a previously selected Sprout, it is promoted to the Sprout state; otherwise, a new Tip cell is selected. The iteration stops when the target number of Sprouts is reached. Finally, in the "Random uniform distribution" model, Tips are selected as Sprouts to maximize their overall spread in the lattice. To implement this constraint, we first select a random Tip and promote it to the Sprout state. Then, the furthest Tip from the newly selected Sprout is selected and promoted to the Sprout state as well. Afterwards, a max-distance function is defined as the sum of pairwise distances between all Sprouts already selected in the lattice. At each following iteration, the Tip cell that maximizes the distance function is selected as a Sprout. The iteration stops when the target number of Sprouts is reached.

Sprout/mini-sprout tracking and analysis

3D vessel chips were kept in a CO_2 incubator at 37 °C and taken out only for imaging at the timepoint depicted in Figures 4A-D. GFP-expressing endothelial cells on a chip at the same position were imaged with a 20x water-immersion objective attached to Lecia scanning disk confocal microscope. IMARIS (Bitplane) was used to separate all newly formed vessels from the

parental vessel and to label them with different colors depending on lumen formation: sprout and mini-sprout. The positions of sprouts and mini-sprouts were simply marked with red and blue squares, respectively (Figs. 4E-H). Then the appearance, disappearance, or the transition from blue to red squares were recorded and tracked throughout the time points. Data from two independent samples were combined to plot the Sankey diagram demonstrating the dynamic change of sprouts and mini-sprouts (Fig. 4I). The analysis was performed using the Python graphing library Plotly.

Immunofluorescence staining of Fibronectin and analysis

All reagents for fibronectin immunostaining were injected through the vessel on a chip and kept as follows: 4% (wt/wt) formaldehyde for 1 hour, 0.1% triton-X for 1hour, 10% goat serum for 1hour, fibronectin antibody (Abcam) at 1:50 dilution for 1 day, secondary antibody (anti-rabbit 594 Thermo Scientific) at 1:100 dilution with Hoechst at 1/200 dilution for 1 day. 3D volumes at 10 positions from two independent samples of VEGF 100 ng/ml treatment and 2 positions from control (No treatment) were imaged with a 20x water-immersion objective attached to a Lecia scanning disk confocal microscope. Cells on the parental vessel were identified by GFP expression in the cytoplasm (Fig. 6E), then segmented (Fig. 6F) with IMARIS (Bitplane). The averaged fibronectin intensity value of each 3D cell volume and its position were acquired in IMARIS, then each cell was marked as a circle at the corresponding x and y positions (Fig. 6G). The averaged fibronectin intensity values and positions of sprouts and mini-sprouts were acquired by identifying cells as surface entities in IMARIS. The averaged fibronectin intensity values of sprouts (following cell) and mini-sprouts were marked as squares at the corresponding x and y positions (Fig. 6G). 10 sprouts, 11 mini-sprouts induced by VEGF 100 ng/ml, and 10 quiescent cells without VEGF treatment were selected to compare fibronectin intensity values (Fig. 6H). Sprouts often had two compartments of a leading cell and following cells where lumenization occurs. We distinguished the leading sprout and the following sprout for the fibronectin intensity comparison (Fig. 6H). If a sprout was composed of a single cell with lumen, the cell was classified as the following cell. 7 neighboring cells including a sprout, a mini-sprout, or only quiescent cells in each image were grouped (Fig. 6I) to analyze the distribution of the ratio of cells having fibronectin levels higher than a threshold value of 30 (dashed line in Fig. 6H). From 10 images, 42 groups were acquired and used for the analysis (Fig. 6J).

Statistical analysis

One-way ANOVA was performed in GraphPad Prism 9.0.0 followed by Tukey's multiple comparisons test. Differences between pairs were concluded to be significant if they had adjusted p values less than 0.05.

Funding statement

This work was supported by NIH through NCI U54 CA209992 (to A.L.); Mia Neri Foundation (to T.-Y.K.); The Center for Theoretical Biological Physics sponsored by the NSF (Grant PHY-2019745), NSF-PHY-2210291, CPRIT Scholar in Cancer Research sponsored by the Cancer Prevention and Research Institute of Texas (to J.N.O.); a Simons Foundation grant 594598 (to Q.N.). F.B. was supported by a National Science Foundation grant DMS1763272 (Q.N.).

1. R. H. Adams, K. Alitalo, Molecular regulation of angiogenesis and lymphangiogenesis. *Nat Rev Mol Cell Biol* **8**, 464-478 (2007).
2. M. Potente, H. Gerhardt, P. Carmeliet, Basic and therapeutic aspects of angiogenesis. *Cell* **146**, 873-887 (2011).
3. R. Benedito *et al.*, The notch ligands Dll4 and Jagged1 have opposing effects on angiogenesis. *Cell* **137**, 1124-1135 (2009).
4. R. Blanco, H. Gerhardt, VEGF and Notch in tip and stalk cell selection. *Cold Spring Harb Perspect Med* **3**, a006569 (2013).
5. W. Y. Wang, D. Lin, E. H. Jarman, W. J. Polacheck, B. M. Baker, Functional angiogenesis requires microenvironmental cues balancing endothelial cell migration and proliferation. *Lab Chip* **20**, 1153-1166 (2020).
6. J. Liu *et al.*, Synthetic extracellular matrices with tailored adhesiveness and degradability support lumen formation during angiogenic sprouting. *Nat Commun* **12**, 3402 (2021).
7. T. Y. Kang *et al.*, Pericytes enable effective angiogenesis in the presence of proinflammatory signals. *Proc Natl Acad Sci U S A* **116**, 23551-23561 (2019).
8. M. B. Chen *et al.*, On-chip human microvasculature assay for visualization and quantification of tumor cell extravasation dynamics. *Nat Protoc* **12**, 865-880 (2017).
9. D. H. Nguyen *et al.*, Biomimetic model to reconstitute angiogenic sprouting morphogenesis in vitro. *Proc Natl Acad Sci U S A* **110**, 6712-6717 (2013).
10. M. Boareto *et al.*, Jagged-Delta asymmetry in Notch signaling can give rise to a Sender/Receiver hybrid phenotype. *Proc Natl Acad Sci U S A* **112**, E402-409 (2015).
11. F. Bocci, J. N. Onuchic, M. K. Jolly, Understanding the Principles of Pattern Formation Driven by Notch Signaling by Integrating Experiments and Theoretical Models. *Front Physiol* **11**, 929 (2020).
12. Y. Yang *et al.*, Deciphering chemical order/disorder and material properties at the single-atom level. *Nature* **542**, 75-79 (2017).
13. K. Bu *et al.*, Nested order-disorder framework containing a crystalline matrix with self-filled amorphous-like innards. *Nat Commun* **13**, 4650 (2022).
14. D. L. Liu, M. An, I. R. Johnson, J. V. Lovett, Mathematical Modeling of Allelopathy. III. A Model for Curve-Fitting Allelochemical Dose Responses. *Nonlinearity Biol Toxicol Med* **1**, 37-50 (2003).
15. G. S. Fraenkel, The raison d'etre of secondary plant substances; these odd chemicals arose as a means of protecting plants from insects and now guide insects to food. *Science* **129**, 1466-1470 (1959).
16. R. J. Willis, *The history of allelopathy* (Springer, Dordrecht, 2007), pp. xiv, 316p. : ill., facsims., map, ports.
17. A. M. Turing, The chemical basis of morphogenesis. 1953. *Bull Math Biol* **52**, 153-197; discussion 119-152 (1990).
18. P. K. Maini, R. E. Baker, C. M. Chuong, Developmental biology. The Turing model comes of molecular age. *Science* **314**, 1397-1398 (2006).
19. X. Feng, M. G. Tonnesen, S. A. Mousa, R. A. Clark, Fibrin and collagen differentially but synergistically regulate sprout angiogenesis of human dermal microvascular endothelial cells in 3-dimensional matrix. *Int J Cell Biol* **2013**, 231279 (2013).
20. A. Senk, V. Djonov, Collagen fibers provide guidance cues for capillary regrowth during regenerative angiogenesis in zebrafish. *Sci Rep* **11**, 19520 (2021).

21. N. D. Kirkpatrick, S. Andreou, J. B. Hoying, U. Utzinger, Live imaging of collagen remodeling during angiogenesis. *Am J Physiol Heart Circ Physiol* **292**, H3198-3206 (2007).
22. M. Galbraith, F. Bocci, J. N. Onuchic, Stochastic fluctuations promote ordered pattern formation of cells in the Notch-Delta signaling pathway. *PLoS Comput Biol* **18**, e1010306 (2022).
23. Y. L. Koon, S. Zhang, M. B. Rahmat, C. G. Koh, K. H. Chiam, Enhanced Delta-Notch Lateral Inhibition Model Incorporating Intracellular Notch Heterogeneity and Tension-Dependent Rate of Delta-Notch Binding that Reproduces Sprouting Angiogenesis Patterns. *Sci Rep* **8**, 9519 (2018).
24. J. R. Collier, N. A. Monk, P. K. Maini, J. H. Lewis, Pattern formation by lateral inhibition with feedback: a mathematical model of delta-notch intercellular signalling. *J Theor Biol* **183**, 429-446 (1996).
25. H. Shin, D. J. Reiner, The Signaling Network Controlling C. elegans Vulval Cell Fate Patterning. *J Dev Biol* **6** (2018).
26. A. S. Yoo, C. Bais, I. Greenwald, Crosstalk between the EGFR and LIN-12/Notch pathways in C. elegans vulval development. *Science* **303**, 663-666 (2004).
27. Y. Zhang *et al.*, Oscillations of Delta-like1 regulate the balance between differentiation and maintenance of muscle stem cells. *Nat Commun* **12**, 1318 (2021).
28. O. F. Venzin, A. C. Oates, What are you synching about? Emerging complexity of Notch signaling in the segmentation clock. *Dev Biol* **460**, 40-54 (2020).
29. R. Kageyama, Y. Niwa, H. Shimojo, T. Kobayashi, T. Ohtsuka, Ultradian oscillations in Notch signaling regulate dynamic biological events. *Curr Top Dev Biol* **92**, 311-331 (2010).
30. B. Ubezio *et al.*, Synchronization of endothelial Dll4-Notch dynamics switch blood vessels from branching to expansion. *Elife* **5** (2016).
31. H. Shimojo, T. Ohtsuka, R. Kageyama, Oscillations in notch signaling regulate maintenance of neural progenitors. *Neuron* **58**, 52-64 (2008).
32. E. S. Wijelath *et al.*, Heparin-II domain of fibronectin is a vascular endothelial growth factor-binding domain: enhancement of VEGF biological activity by a singular growth factor/matrix protein synergism. *Circ Res* **99**, 853-860 (2006).
33. S. Astrof, R. O. Hynes, Fibronectins in vascular morphogenesis. *Angiogenesis* **12**, 165-175 (2009).
34. K. J. Bayless, R. Salazar, G. E. Davis, RGD-dependent vacuolation and lumen formation observed during endothelial cell morphogenesis in three-dimensional fibrin matrices involves the alpha(v)beta(3) and alpha(5)beta(1) integrins. *Am J Pathol* **156**, 1673-1683 (2000).
35. R. Alon *et al.*, TNF-alpha binds to the N-terminal domain of fibronectin and augments the beta 1-integrin-mediated adhesion of CD4+ T lymphocytes to the glycoprotein. *J Immunol* **152**, 1304-1313 (1994).
36. S. Guo, M. Z. Sun, X. Zhao, Wavelength of a Turing-type mechanism regulates the morphogenesis of meshwork patterns. *Sci Rep* **11**, 4813 (2021).
37. H. Xu, M. Sun, X. Zhao, Turing mechanism underlying a branching model for lung morphogenesis. *PLoS One* **12**, e0174946 (2017).
38. S. A. Vilchez Mercedes *et al.*, Decoding leader cells in collective cancer invasion. *Nat Rev Cancer* **21**, 592-604 (2021).

39. O. Stassen, T. Ristori, C. M. Sahlgren, Notch in mechanotransduction - from molecular mechanosensitivity to tissue mechanostasis. *J Cell Sci* **133** (2020).
40. M. Boareto, M. K. Jolly, E. Ben-Jacob, J. N. Onuchic, Jagged mediates differences in normal and tumor angiogenesis by affecting tip-stalk fate decision. *Proc Natl Acad Sci U S A* **112**, E3836-3844 (2015).

Figures

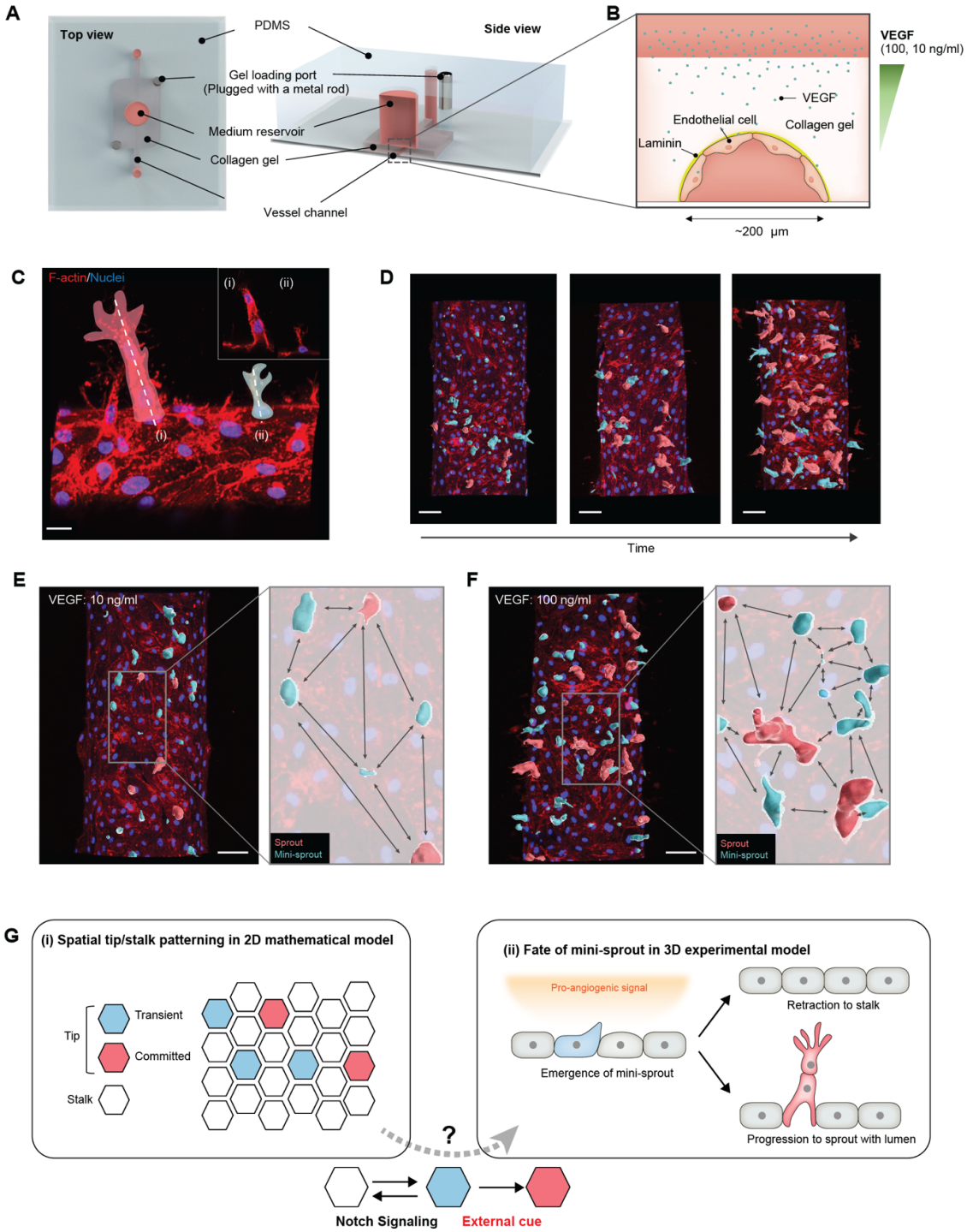

Figure 1. **Analysis of temporal and spatial regulation of angiogenic fate specification in a 3D biomimetic experimental setup**. (A) 3D vessel model for inducing angiogenesis in response to a gradient of VEGF. (B) Cross-section of a vessel embedded in collagen type I within the device; VEGF is added to the medium reservoir above the vessel to generate a VEGF gradient. (C)

Angiogenesis leads to *de novo* formation of sprout-related structures from the parental vessel that have two distinct morphologies: (i) full-fledged multi-cellular sprouts containing detectable lumens, (ii) mini-sprouts in the form of single cell extension into the matrix. Scale bars: 20 μm. (D) Temporally resolved observation of dynamic formation of sprouts and mini-sprouts populations during angiogenesis. As depicted in (C), sprouts are pseudo-labeled with red color and mini-sprouts in blue color. Scale bars: 50 μm. Dependence of the spatial distribution of sprouts and mini-sprouts on the VEGF concentration: (E) 10 ng/ml and (F) 100 ng/ml. Scale bars: 50 μm. Images are 3D reconstructions of confocal z-stacks, showing nuclear (DAPI) and cytoskeleton (Phalloidin). (G) Schematic overview of Tip-Stalk patterning: (i) Spatial Tip-Salk patterning due to juxtacrine Notch signaling that might lead to fixed persistent and transient cell fate specification. (ii) Fates of mini-sprouts in experiments: both retraction (thus conversion from the phenotypically Tip to as Stalk phenotype) and stabilization and growth to a fully defined sprout are observed.

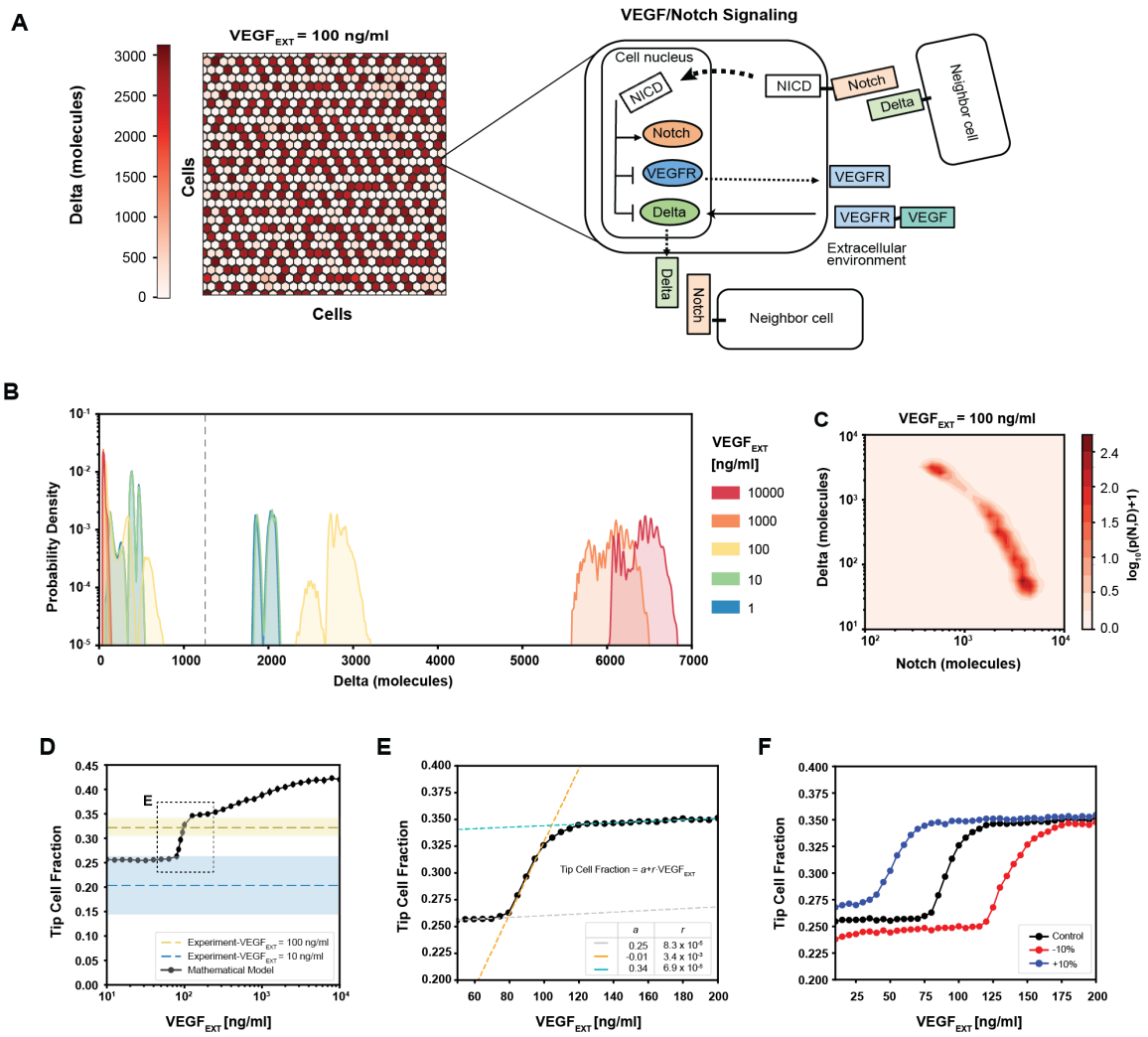

Figure 2. Robust differentiation and order-disorder transition are suggested by mathematical and experimental analyses. (A) Right: An example of a pattern after full equilibration on a 30x30 hexagonal lattice. Color scale highlights the intracellular levels of Delta. Left: The circuit schematic highlights the components of the intracellular Notch-VEGF signaling network. (B) Distribution of intracellular Delta levels in the two-dimensional lattice for increasing levels of external VEGF stimuli. (C) Pseudopotential landscape showing the distribution of intracellular levels of Notch and Delta for $VEGF_{EXT}$=100 ng/ml. (D) Fraction of Tip cells as a function of external VEGF stimulus (black curve). Blue and yellow lines and shading depict experimental fractions of Tip cells for $VEGF_{EXT}$=10 ng/ml and $VEGF_{EXT}$=100 ng/ml, respectively. (E) Detail of Tip cell fraction transition zone (corresponding to box in panel D). Legend depicts the coefficients of the linear fits. (F) Shift of the $VEGF_{EXT}$ transition threshold upon variation of the Notch-Delta binding rate constant. For panels B-F, results are averaged over 50 independent simulations starting from randomized initial conditions for each $VEGF_{EXT}$ level (See Methods section: Simulation details).

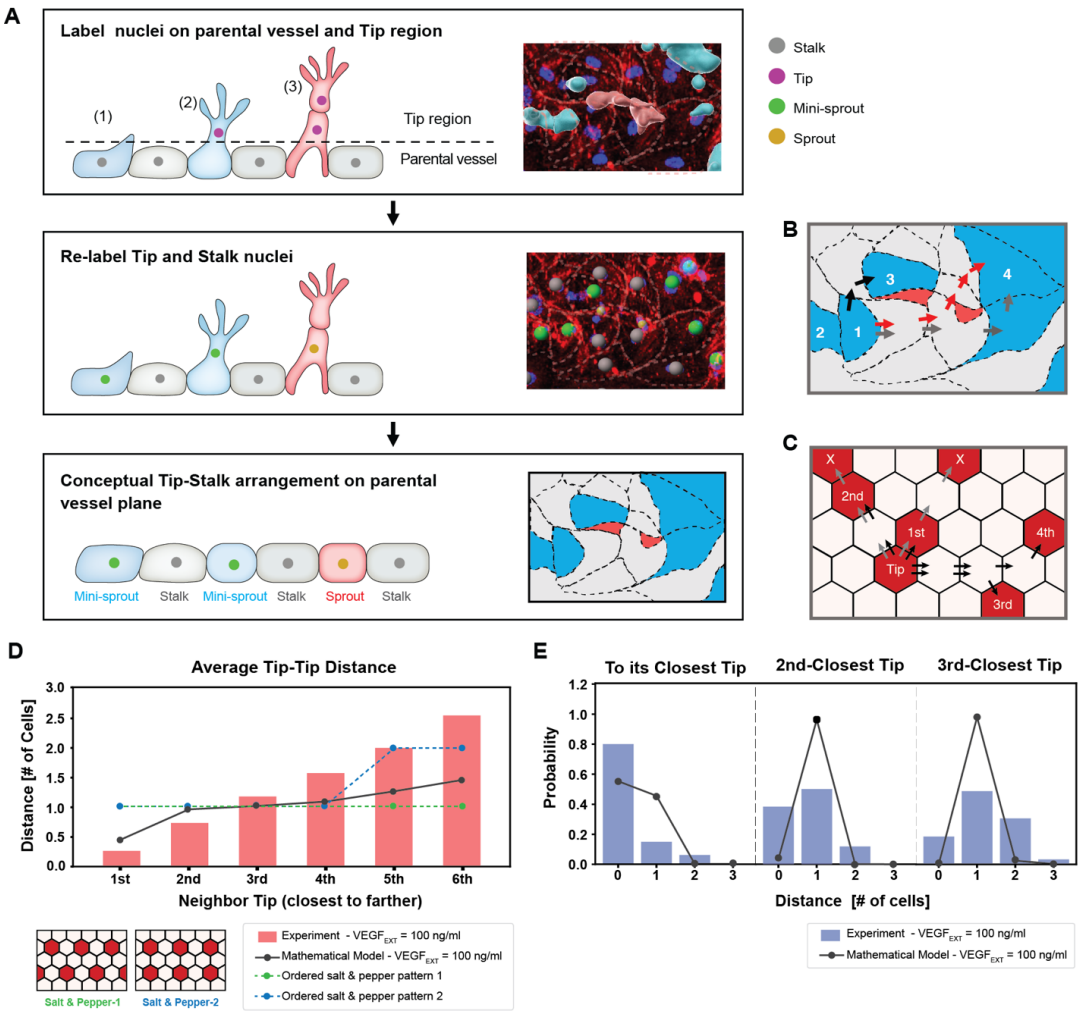

Figure 3. Experimentally measured spatial distribution of Tip cells defined as constituting mini-sprouts and leading sprouts is consistent with the mathematical model predictions. (A) Analysis pipeline to infer the 2D Tip-Stalk arrangements from 3D experimental images: experimental labeling of the nuclei of sprout/mini-sprout cells (above the plane of the parental vessel) and of the Stalk cells (below the plane of the parental vessel) is used to 'compress' the cells in each spout or mini-sprout into a single Tip cell. Tip-Tip distance is defined as the number of cells measured in 'cell hops', i.e., the minimal number of intermediate cells between randomly chosen pairs of Tip cells from experiments (B) (the example is identical to the inset at the bottom of (A)) and 2D Tip-Stalk patterns from mathematical modeling (C). Black arrows indicate minimal and valid cell hops between tips, whereas grey arrows indicate minimal but invalid cell hops (passing through other Tip cells); red arrows indicate the non-minimal cell hops which does not count in the Tip-Tip distance quantification. (D) Tip cell distance distribution from any given Tip cell. Red bars depict experimental measurement for $VEGF_{EXT}$=100 ng/ml and black line depicts the model's prediction for $VEGF_{EXT}$=100 ng/ml. For reference, dashed lines indicate the expected Tip-Tip distance distribution of "perfect" salt-and-pepper patterns shown in the inserts. (E) Detailed distance distribution for the closest Tip (left), second closest Tip (middle), and third closest Tip (right).

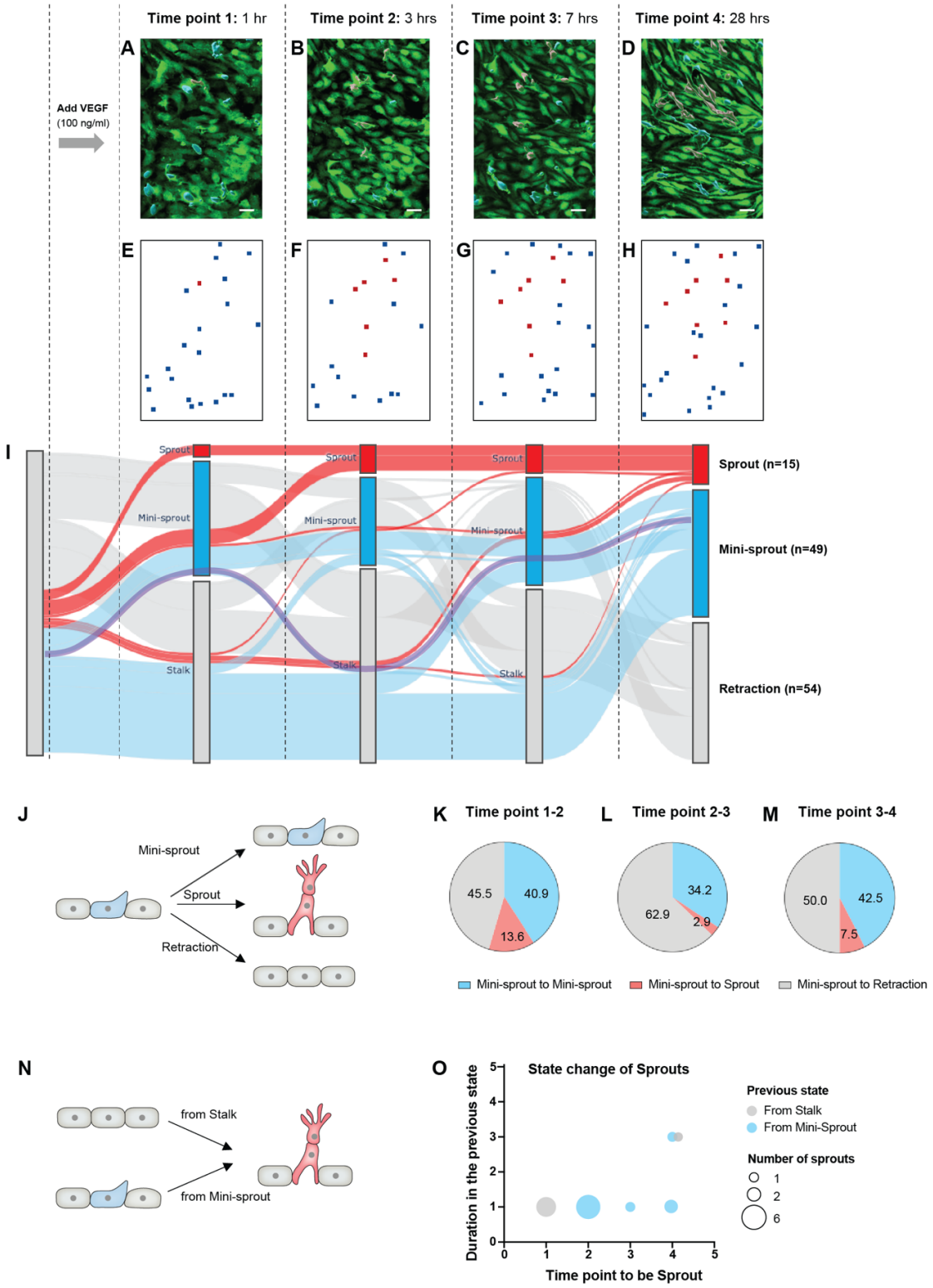

Figure 4. The dynamics of mini-sprout and sprout formation suggest frequent mini-sprout retractions, sit only a subset of mini-sprouts becoming fully formed sprouts. GFP-expressing endothelium in the 3D vessel setup captured 1 hour (A), 3 hours (B), 7 hours (C), and 28 hours

(D) after 100 ng/ml of VEGF treatment. Sprouts and mini-sprouts are identified by red and blue surface entities, respectively. Square marks representing the positions of sprouts (red) and mini-sprouts (blue) in the original images at each time point (E-H). (I) Sankey diagram demonstrating the dynamic state change of sprouts with red lines and mini-sprouts with blue lines throughout the time points. And grey lines represent mini-sprouts which ended up being retracted at the last observation, time point 4. A purple line shows an example of the state change from a Stalk (initially non-invading endothelial cell) to mini-sprout, retraction, mini-sprout, and mini-sprout at each time point. Only cells that that became mini-sprout at least once during the experiment are shown. (J) Different types of observed transitions between consecutive time points when starting from the mini-sprout state: maintain the mini-sprout state, become a sprout, or retract to the stalk state. The ratio of states switched from mini-sprouts in the previous time point 1 (K), time point 2 (L), and time point 3 (M). (N) The two observed pathways to sprout formation between consecutive time points: direct Stalk to sprout or mini-sprout to sprout transition. Once a newly formed vessel becomes a sprout, it is permanently committed. (O) Duration of staying as a mini-sprout or a Stalk in the previous state before being committed to a sprout.

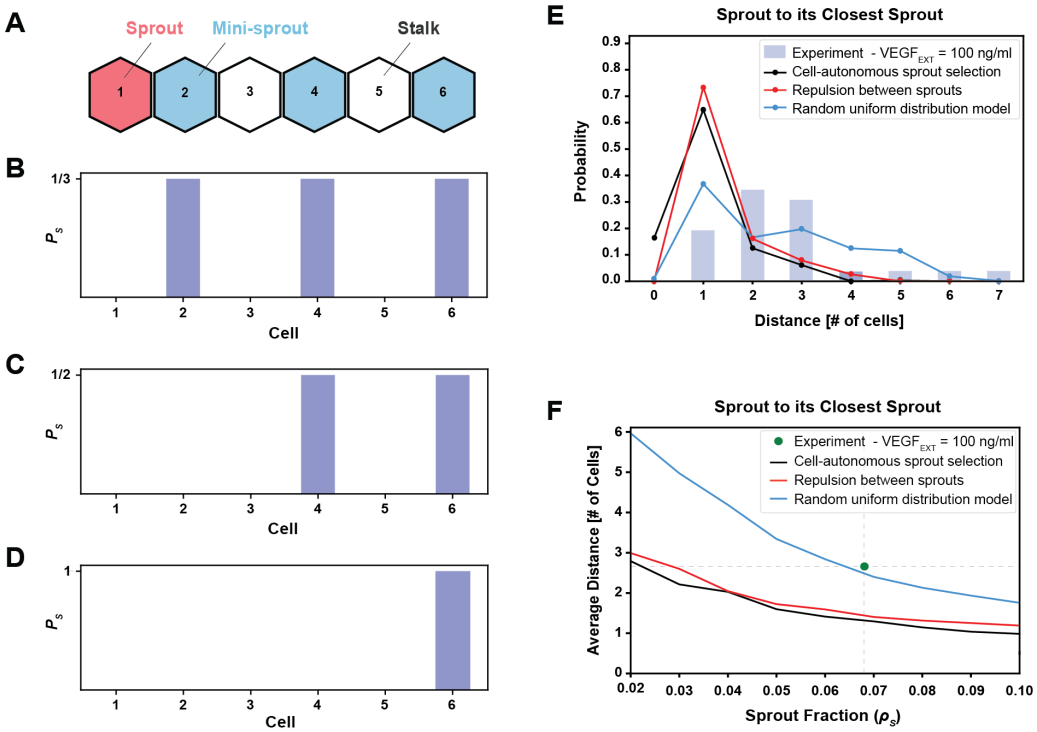

Figure 5. The phenomenological model favoring maximal sprout-sprout distances for a given number of sprouts (random uniform distribution) is most consistent with the experimental observations. (A) An example of 1-dimenstional Tip cell distribution, including a sprout and mini-sprouts, and Stalks pattern. (B) Sprout selection probability (P_S) for the cell-autonomous model if a new sprout was added to the pattern of (A). Stalk cells cannot become sprouts, and existing mini-sprouts share the same selection probability. (C) Sprout selection probability (P_S) for the sprout repulsion model. The leftmost mini-sprout cannot be selected because it is already in contact with an existing sprout, while the remaining two mini-sprouts share the same selection probability. (D) Sprout selection probability (P_S) for the random uniform distribution model. The rightmost mini-sprout maximizes the distance to the existing sprout and is therefore the only viable selection. (E) Sprout distance distribution to its closest sprout neighbor. Blue bars indicate experimental results for $VEGF_{EXT}$=100 ng/ml while black, red and blue lines depict the three different models of sprout selection (cell-autonomous, repulsion between sprouts, and random uniform distribution, respectively). (F) Average distance between a sprout and its closest sprout neighbor in the model as a function of sprout cell fraction in the lattice for the three proposed models of sprout selection. The green dot highlights the experimental sprout fraction and distance at $VEGF_{EXT}$=100 ng/ml.

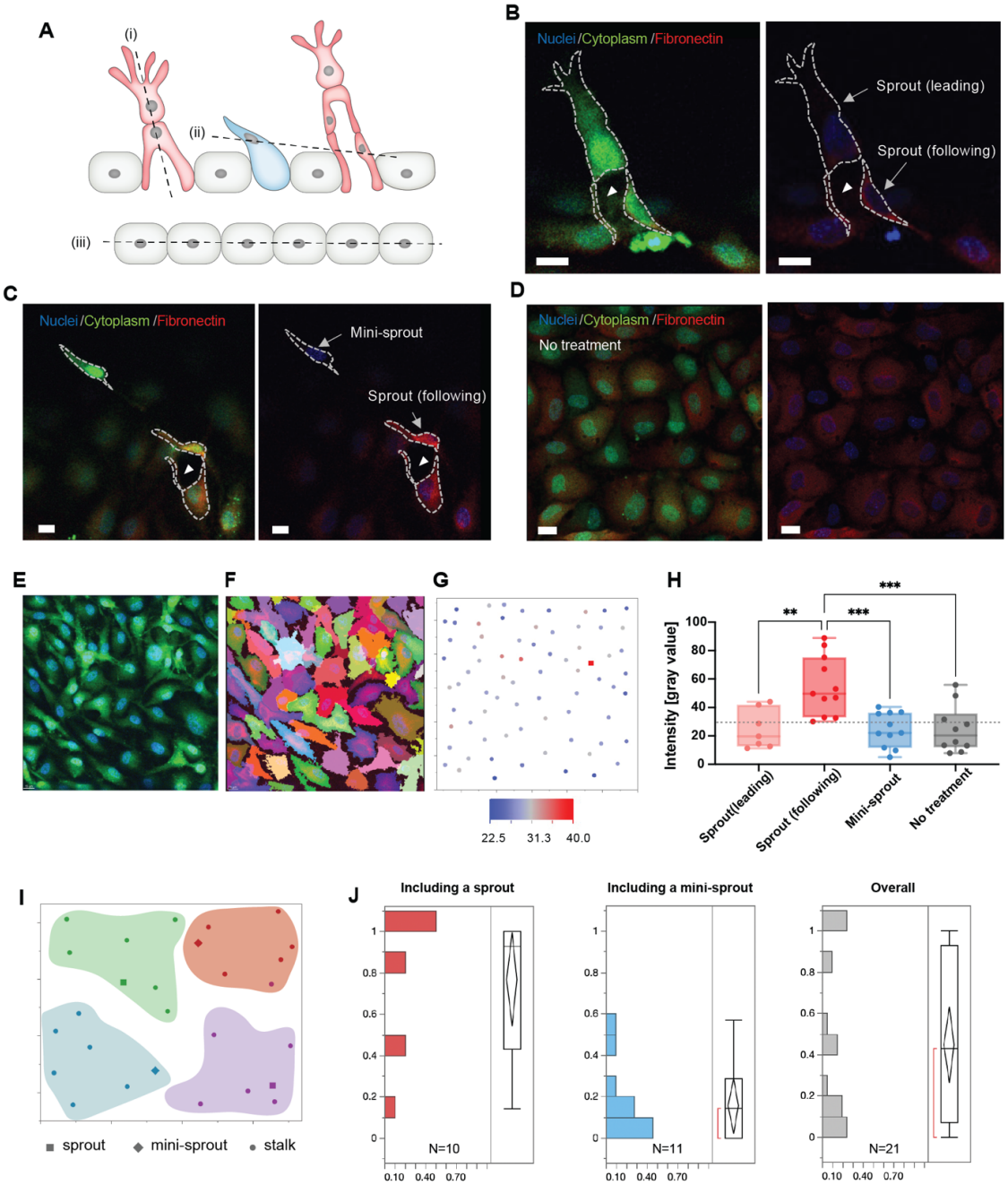

Figure 6. Fibronectin distribution on parental and newly formed vessels reveals preferred distribution at the bases of sprouts. (A) A schematic describing cross-sectional planes for subsequent confocal images: (i) for (B), (ii) for (C), and (iii) for (D). (B) Localization of fibronectin expression to a following cell than in a leading cell in a sprout. (C) Higher fibronectin expression in a sprout (a 'following' cell at the base of the sprout) than at a mini-sprout. (D) Intrinsic heterogeneity of fibronectin expression on quiescent endothelium displaying no mini-sprout or sprout formation. Images are 3D reconstructions of confocal z-stacks. Scale bars: 15 μm. Cells on the parental vessel were identified by GFP expression in the cytoplasm (E), then segmented

(F). (G) Fibronectin intensity of each cell on the parental vessel is marked as a dot at the corresponding x and y positions,of the cell centroids. Fibronectin intensities for sprouts (following cells) or mini-sprouts are indicated as squares. (H) Fibronectin intensity of leading cells and following cells of sprouts, mini-sprouts, and quiescent cells. (I) Cellular layer was segmented into groups containing 7 neighboring cells to assess the local environment for each group. (J) Distributions of the ratio of cells having fibronectin levels higher than a threshold, the minimum value of sprout in (H), in a group of 7 neighboring cells defined in (I), which included either a sprout or a mini-sprout. The overall distribution covers both regions.

Sprout	
	Early Stage I Multi-cells face each other and form a lumen.
	Early Stage II Luminization occurs within a migrating cell.
	Matured Stage A leading cell is followed by multiple cells with a lumen.
Mini-sprout	
	Cells change polarity and migrate but luminization is not observed.

Table 1. Phenotypic categorization of sprout and mini-sprout.

Parameter type	Parameter	Value	Units
Production	N_0, D_0, J_0, V_{R0}	1200,1000,800, 1000	Molecule/hour
Degradation	γ, γ_I	0.1, 0.5	1/hour
Binding	k_T, k_C	2.5 10^{-5}, 5 10^{-4}	1/(molecule hour)
Hill threshold	I_0, V_0	200, 80*	Molecules
Fold-change	λ_N, $\lambda_{I,D}$, $\lambda_{V,I}$, λ_J, λ_V	2, 0, 0, 2, 2	Dimensionless
Hill coefficient	n_N, $n_{I,D}$, $n_{V,I}$, n_J, n_V	2, 2, 2, 5, 2	Dimensionless

Table 2. Parameter values for simulation. *Rescaled from previous model to match experimental observation.